RSC Advances

PAPER

View Article Online
View Journal | View Issue

Cite this: *RSC Adv.*, 2025, **15**, 6863

Scrutinization of late first-row transition metals decorated octagonal boron (B8) ring complexes as single-atom catalysts for green hydrogen and oxygen production†

Naveen Kosar, *[a] Tariq Mahmood, *[b] Muhammad Arshad, [c] Muhammad Imran [d] and Utkirjon Holikulov[e]

Received 10th October 2024
Accepted 25th February 2025

DOI: 10.1039/d4ra07274j

rsc.li/rsc-advances

Hydrogen as fuel has gained large interest nowadays as a green energy source. Single-atom catalysis has emerged as a promising strategy for producing hydrogen. Herein, we investigated the late first row transition metals (TM = Co, Cu, Zn, Ni and Fe) adsorbed on eight-membered boron ring (TM@B8) as potential single-atom catalysts (SAC) towards hydrogen evolution reaction (HER) as well as oxygen evolution reaction (OER), aiming to identify less expensive electrocatalysts with high efficiency. Various properties including interaction energy (E_{int}), energies of frontier molecular orbitals (FMOs), natural bonding orbital (NBO) charges, total density of state (TDOS) spectra and non-covalent interaction (NCI) analyses of considered complexes are explored. These findings demonstrated that both pure TM@B8 and hydrogen-adsorbed TM@B8 complexes have both structural and electronic stability. The Co@B8 complex demonstrated a favorable Gibbs free energy of 0.16 eV toward HER under gaseous conditions. Fe@B8 showed better OER activity having overall η_{OER} of 1.14 eV. These outcomes show the promising potential of TM@B catalysts for both HER and OER processes.

1 Introduction

Boron's ability to form multiple bonds enables the synthesis of diverse boranes with unique geometric and electronic properties.[1,2] Boranes have applications as chemical insulators,[3] high-modulus fiber composites,[4] semiconductors,[5] refractory materials[6] and high energy density fuels[7] *etc.* Recently, boron nanoclusters (B6, B8, B38 and B40 *etc.*) are reported in literature and gained attention due to their thermodynamic stability, electron deficiency, large surface area, low density, high coordination number and covalent nature.[8,9] B8 exhibits excellent semiconducting, optical, and catalytic properties. Doping of external metal further enhances the stability, magnetic properties, and electronic transmutation of resultant B8 complexes as evident from various literature reports.[10,11]

Single atom catalysis (SAC) is a rapidly advancing field across scientific disciplines, where metal atoms are deposited on a chemical surface to enhance catalytic efficiency.[12–14] The atomic size of a metal plays a crucial role in determining catalyst performance. As the size of the metal particles decreases, the activity increases, alongside an increase in surface free energy that discourages aggregation into larger clusters.[12] Sun *et al.* used atomic layer deposition (ALD) technique to experimentally synthesize single atom based platinum (Pt) doped graphene sheet and observed better catalytic performance than commercial Pt/C catalyst.[15] Shui and coworkers synthesized rare earth metals (yttrium and scandium) doped carbon supported SACs for carbon and nitrogen reduction at room temperature.[16]

Recently, there has been growing interest toward hydrogen evolution reaction (HER) and oxygen evolution reaction (OER) using single-atom catalysis.[17,18] Hydrogen production through HER is an endergonic process, the sustainability of which depends on the suitable catalyst, reactants, and efficient energy sources. Scientists have assigned color codes to classify hydrogen based on the level of sustainability. Currently, small amounts of "low-carbon hydrogen" are produced through water electrolysis using nuclear power (purple hydrogen) or grid electricity (yellow hydrogen).[19] The production of truly green hydrogen, however, requires a combination of renewable

[a]*Department of Chemistry, University of Management and Technology (UMT), C-11, Johar Town, Lahore, Pakistan. E-mail: naveen.kosar@umt.edu.pk*

[b]*Department of Chemistry, COMSATS University Islamabad, Abbottabad Campus, Abbottabad 22060, Pakistan. E-mail: mahmood@cuiatd.edu.pk*

[c]*Institute of Chemistry, The Islamia University of Bahawalpur, Baghdad-ul-Jadeed Campus, Bahawalpur, 63100, Pakistan*

[d]*Research Center for Advanced Materials Science (RCAMS), Chemistry Department, Faculty of Science, King Khalid University, P. O. Box 9004, Abha 61413, Saudi Arabia*

[e]*Department of Optics and Spectroscopy, Samarkand State University, 15 University Blvd, Samarkand 140104, Uzbekistan*

† Electronic supplementary information (ESI) available. See DOI: https://doi.org/10.1039/d4ra07274j

feedstocks, efficient SACs and efficient energy sources, ideally sunlight.[20–23] SACs can lower the overpotential, larger activation barriers and slow kinetics processes. Extensive research has been carried out over the last few years to identify SACs having outstanding efficiency toward green HER. Experimentally, HER electrocatalysis is multi-step process including the transfer of two electrons on metallic surface. The whole reaction occurs under various pH conditions: alkaline,[24] acidic[25] and neutral media.[26] Jousselme and coworkers synthesized non-noble metal single-atom catalysts from carbonized metal-doped ZIFs, exhibiting high activity and stability toward hydrogen evolution achieving −322 mV overpotential at −10 mA cm^{-2} in acidic media.[27] HER under alkaline medium enhances metal stability and address safety and cost concerns associated with acidic conditions.[28] Kim *et al.* described the improvement of HER activity in the presence of alkaline electrolyte.[29] Hydrogen production *via* HER under extreme pH conditions faces severe challenges, and sustainable strategy to overcome those involves utilizing neutral or near-neutral electrolytes for HER. Sun *et al.* demonstrated theoretically as well as experimentally that nitrogen-doped porous Ni framework exhibited exceptional electrocatalytic performance toward HER under neutral conditions (pH 7) and achieved a current density of 10 mA cm^{-2} along with low overpotential of 64 mV. These substantial experimental reports demonstrate the effectiveness of transition metal-based SACs toward HER.

Experimental approaches to validate HER activity of catalysts include valence band photoelectron spectroscopy, electrochemistry, and advanced spectroscopic techniques. Theoretical concepts such as adsorption free energy, microkinetic models, volcano plots, and d-band centers are widely employed for the (semi)quantitative evaluation of HER electrocatalysts.[30] Pt is the benchmark HER electrocatalyst due to its high exchange current density in one direction (j_0) at equilibrium potential and low Tafel slope.[31] According to Sabatier principle, the HER free energy diagram evaluates H* adsorption/desorption *via* ΔG_{H^*},[32] which should ideally approach zero for maximum reaction rate (this ideal Tafel step facilitates both adsorption and desorption of hydrogen). More than zero value of ΔG_{H^*} represents weak hydrogen adsorption (Volmer step) and less than zero represents strong hydrogen adsorption (Heyrovsky step).[33] First-principle calculations allow the construction of HER free-energy diagrams, revealing the thermodynamic favorability of specific reaction pathways on various catalyst surfaces. A correlation between experimental j_0 and computed ΔG_{H^*} is observed as a "volcano curve," correlating catalyst surface properties to HER kinetics.[34] DFT studies reveal that in MoS_2, only the S–Mo–S edge sites are active for H* adsorption, with [1010] Mo edges showing ΔG_{H^*} comparable to Pt.[35] Electrochemical and STM studies validate this, demonstrating j_0 proportionality to edge length rather than basal plane area.[36] Similarly, g-C_3N_4 with nitrogen-doped graphene exhibits higher j_0 along with lower overpotential (η) and near-zero ΔG_{H^*}, enhancing HER activity.[37] In addition to the free energy level of each reaction step (reactant, intermediates, and final product), the possible reaction barriers can also affect the overall reaction rate. The calculation of reaction barriers for the Tafel step at both equilibrium potential and certain overpotential are achievable just by including n_e and η for each step (n_e denotes the electron numbers carried by the electrode surface and η is the overpotential of the electrode). Such insights are critical for designing and optimizing electrocatalysts by tuning electronic structure and surface chemistry.

Herein, we designed and executed DFT based work to study the late first row transition metals (Zn, Cu, Co, Ni, Fe) doped B8 nanoclusters as single atom catalysts (SACs) toward HER (see Fig. 1). We hope B8 nanocluster with first row transition metals can act as better road map toward SACs for HER. Besides HER, oxygen evolution reaction (OER) potential is also investigated using the same transition metals doped B8 SACs as in literature there are number of SACs are also used to investigate their OER activity.[38–40]

2 Computational methods

The structures are built in GaussView 5.0 software,[41] and subsequently simulation are processed in Gaussian 09 software.[42] By building, optimizing, and computing the molecular model, key properties such as energy, bond lengths, charge distribution, atomic and molecular orbitals can be obtained. Gaussian simulations are highly powerful and widely used for calculating molecular electronic structures and spectral characteristics. ωB97XD functional of DFT and Pople's 6-31+G(d,p) basis set are used in these calculations. The energy minima structures of isolated B8 and selected transition metals (Zn, Cu, Co, Ni, Fe) doped B8 complexes are obtained from these calculations both in gas phase and solvent phase (water). Interaction energy (E_{int}) and Gibbs free energy are also calculated for the validation of thermodynamic stability of the complexes under neutral conditions as well as under aqueous conditions. E_{int} of all designed complexes is calculated by using the following eqn (1):

$$E_{int} = E_{(B8+TM)} - (E_{B8} + E_{TM}) \quad (1)$$

Here, $E_{(B8+TM)}$, E_{B8} and E_{TM} are the notations for the energy of transition metal (TM = Zn, Cu, Co, Ni, Fe) doped B8, the energy of pure B8 and the energy of TM, respectively. The energy gap (E_{H-L}), between the highest occupied and the lowest unoccupied molecular orbitals is calculated by using eqn (2).

$$E_{H-L} = E_{LUMO} - E_{HOMO} \quad (2)$$

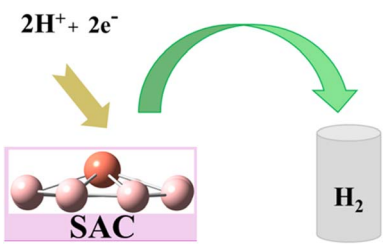

Fig. 1 Schematic diagram showing the proposed mechanism of HER.

The total density of states (TDOS), non-covalent interactions index (NCI) and natural bond orbital (NBO) analyses are studied at ωB97XD/6-31+G(d,p) method. The following half reaction is considered to study the production of hydrogen (eqn (3)).

$$H_{(aq)}^{+} + e^{-} \rightarrow \frac{1}{2}H_{2(g)} \quad (3)$$

Zero-point corrected energies (ΔE_{ZPE}) are used for the estimation of change in Gibbs free energy (ΔG_H) and change in enthalpies (ΔE_H). These parameters (ΔG_H, ΔE_H ΔE_{ZPE}) at absolute temperature (at 298.15 K and 1 atm pressure) are calculated through eqn (4)–(6):

$$\Delta G_H = \Delta E_H + \Delta E_{ZPE} - T\Delta S_H \quad (4)$$

$$\Delta E_H = E_{(B8+TM+H)} - \left(E_{(B8+T)} + \frac{1}{2}E_{H_2}\right) \quad (5)$$

$$\Delta E_{ZPE} = E_{ZPE(B8+TM+H)} - \left(E_{ZPE(B8+TM)} + \frac{1}{2}E_{ZPE(H_2)}\right) \quad (6)$$

We also examined the oxygen evolution reaction (OER) through four proton-coupled electron transfer mechanism as shown below as steps (I)–(IV):

$$TM@B8 + H_2O \rightarrow TM@B8\text{–}OH + H^+ + e^- \quad (I)$$

$$TM@B8\text{–}OH \rightarrow TM@B8\text{–}O + H^+ + e^- \quad (II)$$

$$TM@B8\text{–}O + H_2O \rightarrow TM@B8\text{–}OOH + H^+ + e^- \quad (III)$$

$$TM@B8\text{–}OOH \rightarrow TM@B8 + O_2 + H^+ + e^- \quad (IV)$$

The variation in Gibb's free energy values of the PCET steps (I)–(IV) is calculated by using eqn (7)–(10) to estimate further the overall OER potential.

$$\Delta G_I = G_{TM@B8\text{–}OH} + 1/2G_{H_2} - (G_{TM@B8} + G_{H_2O}) \quad (7)$$

$$\Delta G_{II} = G_{TM@B8\text{–}O} + 1/2G_{H_2} - G_{TM@B8\text{–}OH} \quad (8)$$

$$\Delta G_{III} = G_{TM@B8\text{–}OOH} + 1/2G_{H_2} - (G_{TM@B8\text{–}O} + G_{H_2O}) \quad (9)$$

$$\Delta G_{IV} = G_{TM@B8} + G_{O_2} + 1/2G_{H_2} - G_{TM@B8\text{–}OOH} \quad (10)$$

One of the important steps of the PCET steps is the one having highest Gibb's free energy is known as potential determination step (PDS). The PDS is used to estimate the chemical kinetics of the chemical processing, and it is directly related to overpotential (η). The η of OER is calculated by the below given equation:

$$\eta_{OER} = E_{PDS} - E^{\circ} \quad (11)$$

E_{PDS} and E° are denoted by electrochemical potential of PDS and standard electrochemical potential of PDS for the total OER at 298.15 K and 1 atm pressure.

3 Results and discussion

3.1 Geometries and stabilities of pure B8 and TM@B8 complexes

The energy minima structure of B8 consists of an eight-member boron ring having 1.55 Å average B–B bond length. We selected three active sites of B8 nanocluster for transition metals doping including top of B8 ring, middle of B–B bond and top of B atom (see Fig. 2).

Initially considered TM are doped on all considered sites shown in Fig. 2, but after optimization of TM@B8 complexes, the stable orientation is only obtained is the top central position of B8 nanocluster (B8-top), as given in Fig. 3. The B–B bond length of B8 is changed after interacting with TM. The B–B bond length in Fe@B8, Co@B8, Ni@B8, Cu@B8 and Zn@B8 complexes is 1.56, 1.56, 1.57, 1.55 and 1.57 Å, respectively. We also estimated the interaction distance between boron ring and adsorbed transition metals (D_{TM-B8}). The D_{TM-B8} in Fe@B8, Co@B8, Ni@B8, Cu@B8 and Zn@B8 is 2.17, 2.09, 2.06, 2.13 and 2.22 Å, respectively. The interaction distance between TM and

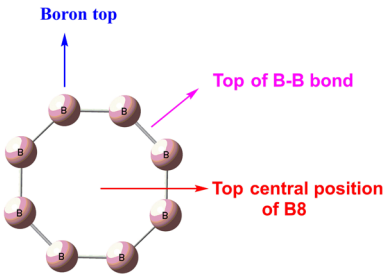

Fig. 2 Optimized geometry of B8 showing the selected sites (B8-top, bond between B–B and top of the B8) for transition metals (TM) doping.

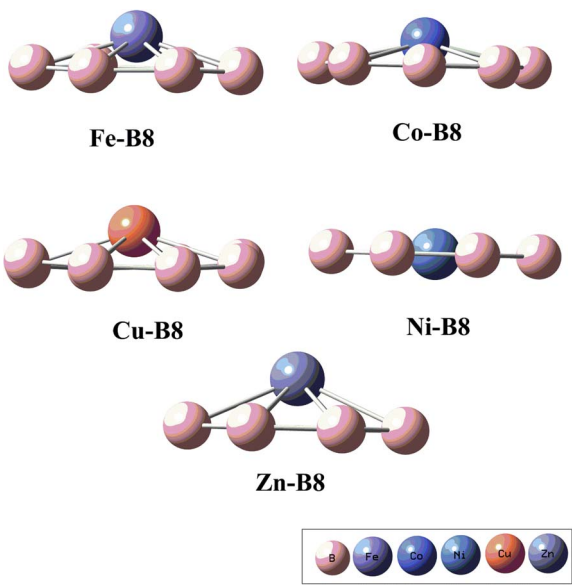

Fig. 3 The optimized geometries of transition metals adsorbed on B8 (TM@B8, TM = Zn, Cu, Co, Ni, Fe).

Table 1 The spin multiplicity and relative energies (E_{rel}, in kcal mol^{-1}) of the different spin states for transition metals (TM) adsorbed on B8

Properties	Spin states	Cu@B8	Zn@B8	Co@B8	Ni@B8	Fe@B8
Multiplicities	Most stable state	Singlet	Triplet	Doublet	Quartet	Triplet
	2nd stable state	Triplet	Singlet	Quartet	Sextet	Quintet
	3rd stable state	Quintet	Quintet	Sextet	Doublet	Singlet
E_{rel}	Most stable state	0.00	0.00	0.00	0.00	0.00
	2nd stable state	13.53	15.59	17.83	22.91	15.68
	3rd stable state	63.02	57.27	36.96	24.66	17.51

B8 is noticeably decreased as the interactive forces are operational between the two species.

The three lowest spin states of each complex are analyzed to identify the most stable spin multiplicity (see Table 1 for relative energies). The most stable states for Zn@B8 and Fe@B8 are triplet. Singlet is observed as the most stable state for Cu@B8, doublet for Co@B8 and quartet for Ni@B8. Compared to the triplet state of Fe@B8, the quintet and singlet states of this complex have relative energies 15.68 and 17.51 kcal mol^{-1} less stable than the triplet state, respectively. The most stable spin state for Co@B8 is the doublet, its quartet and sextet states have relative energy of 17.83 and 36.96 kcal mol^{-1}, respectively compared to doublet spin state. For Ni@B8, the quartet state is the most stable one. The sextet and the doublet states have relative energies of 22.91 and 24.66 kcal mol^{-1} than the quartet one, respectively. In the case of Cu@B8, the singlet spin state is highly stable. Triplet and quintet spin states have relative energies of 13.53 and 63.02 kcal mol^{-1} as compared to singlet. In Zn@B8 complex, the triplet spin state has the highest stability compared to singlet and quintet spin states, those have higher energies of 15.59 and 57.27 kcal mol^{-1} than the triplet state.

Thermodynamic feasibility of all complexes is estimated through interaction energy (E_{int}) calculation. All TM@B8 complexes have higher E_{int}, demonstrating the suitability of TM adsorption on the B8. Co@B8 is the most stable (−0.32 eV), followed by Fe@B8 (−0.26 eV), Ni@B8 (−0.25 eV), Cu@B8 (−0.21 eV), and Zn@B8 (−0.15 eV) (see Table 2). The E_{int} value of complexes under aqueous conditions are −0.30, −10.91, −8.92, −6.29 and −0.17 eV for Fe@B8, Co@B8, Ni@B8, Cu@B8, Zn@B8 respectively (see Table S1, ESI†). The negative value of interaction energy reflects the thermodynamic feasibility of complexation of consider transition metals with B8. The shorter interaction distance between Co and B8 in Co@B8 complex is evident of its highest stability, which is further proved from E_{int} of this complex (−0.32 eV). The larger interaction distance (2.22 Å) between Zn and B8 is in Zn@B8 complex shows the weak complexation, which is supported by low E_{int} of this complex. The E_{int} result of our complexes is similar to the investigation on various 2D nanosheets used for the electrochemical process of the HER.[43]

Table 2 NBO charge of TM in each complex (Q_{TM} in $|e|$), interaction distance between TM & eight-member boron ring (D_{TM-B} in Å), energy gap (E_{gap} in eV), the energies of LUMOs (E_{LUMO} in eV), the energies of HOMOs (E_{HOMO} in eV), interaction energy of single transition metal adsorbed eight-member boron complexes (E_{int} in eV) and interaction distance between boron & boron of the boron ring (D_{B-B} in Å) of TM adsorbed eight membered boron complexes (TM@B8, TM = Zn, Cu, Co, Ni, Fe)

System	Q_{TM}	D_{TM-B}	E_{H-L}	E_{LUMO}	E_{HOMO}	E_{int}	D_{B-B}
B8	0	—	8.71	0.41	−8.29	—	1.55
Fe@B8	−0.48	2.17	5.84	−2.61	−8.45	−0.26	1.56
Co@B8	0.10	2.09	5.74	−2.68	−8.42	−0.32	1.56
Ni@B8	−0.28	2.06	5.36	−2.53	−7.89	−0.25	1.57
Cu@B8	0.35	2.13	5.07	−2.93	−8.00	−0.21	1.55
Zn@B8	0.74	2.22	7.32	−0.83	−8.15	−0.15	1.57

3.2 Electronic properties of pure B8 and TM@B8 complexes

Frontier molecular orbitals (FMOs) analysis is employed to assess the electronic characteristics of B8 and TM@B8 complexes (for values see Table 2). The E_{H-L} of the pure B8 nanocluster is 8.71 eV, which decreases after doping with transition metals. After doping with transition metals, the E_{H-L} for and Zn@B8, Cu@B8, Ni@B8, Co@B8 and Fe@B8 complexes is 7.32, 5.07, 5.36, 5.74 and 5.84 eV, respectively. The E_{H-L} values indicate the semi-conductor nature of TM@B8 complexes and indicate their suitability as electrocatalyst toward HER. The E_{H-L} is decreased due to change in the energies of HOMO and LUMO orbitals. The lowest E_{H-L} of 5.07 eV is seen for Cu@B8 complex, which indicates the increase HOMO energy and decrease of LUMO energy compared to pure B8. Similar behavior is seen for the other complexes except Fe@B8 and Co@B8 complexes, where HOMO energy is increased after complexation. Isodensity in HOMO orbital is located on the bonds between boron atoms and the interaction sites of the boron ring with transition metals, whereas in LUMO orbitals are located primarily on the individual boron atoms of the B8 and to a lesser extent on transition metals (see Fig. S1, ESI†).

Natural bond orbital (NBO) charge analysis revealed the charge transfer between transition metal and B8. NBO charge value on transition metals confirm the direction of charge transfer in B8 complexes (Table 2). NBO charge value on Co, Cu and Zn is 0.10, 0.35 and 0.74$|e|$ in Co@B8, Cu@B8 and Zn@B8 complexes, indicative of transfer of electronic density from metal toward B8. In Fe@B8 and Ni@B8 complexes, the negative charge values on Fe and Ni indicating the shifting of electronic density from B8 surface towards the transition metals. The electronegativity difference of Fe and Co relative to boron is more, which is responsible for withdrawing the electrons from boron and metals act as electron acceptors. Wu and colleagues also observed negative charges during the investigation of HER

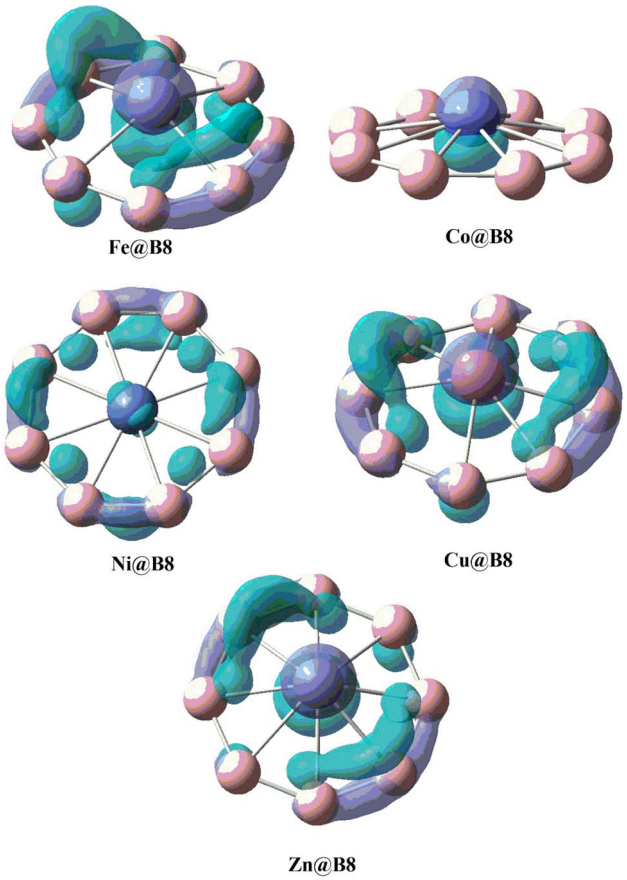

Fig. 4 Graphics of EDD analysis of TM@B8 (TM = Zn, Cu, Co, Ni, Fe) complexes.

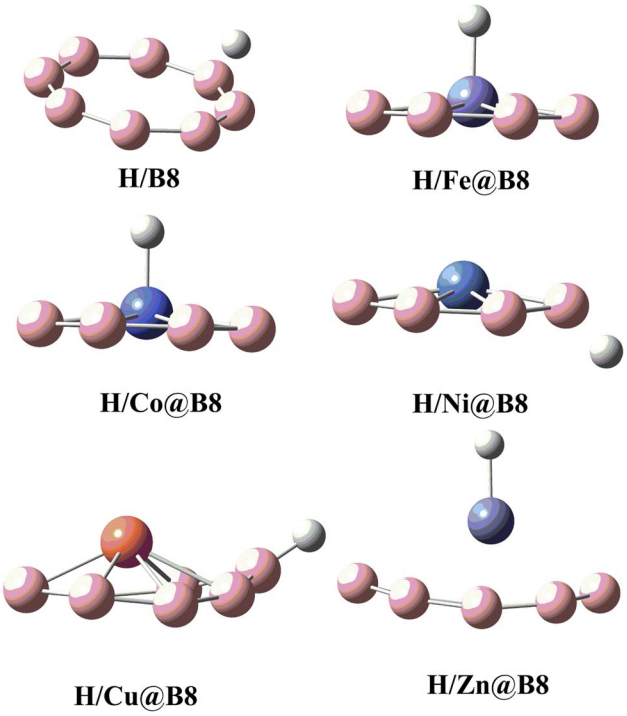

Fig. 5 The optimized geometries of hydrogen adsorbed TM@B8 complexes.

activity of transition metal doped iron sulphide complexes.[44] Janjua also observed the similar trend of NBO charges while working on transition metals adsorbed $Mg_{12}O_{12}$ nanocages.[45]

Electron density distribution (EDD) analysis is performed to observe qualitative indication of charge transfer between TM and B8. Two different colors (cyan blue and purple) as shown in Fig. 4 are indicative of charge transfer. In Fe@B8 and Ni@B8 complexes, purple color on B8 represents the charge transfer from the B8 toward the transition metals. The cyan blue color surface on the interacting site of the TM (Fe and Ni) illustrates the acceptance of charge by TM. In Co@B8, Cu@B8 and Zn@B8 complexes, purple color is on TM (Co, Cu and Zn) represent the charge transfer from the transition metals toward the B8. The cyan blue surface on the interacting site of B8 illustrates the acceptance of charge by B8.

3.3 Geometric and electronic properties of hydrogen adsorbed TM@B8 complexes

For analyzing the HER activity atomic hydrogen (H) is adsorbed on each TM@B8 complex and optimized geometries are shown in Fig. 5. Both the transition metal and boron act as cationic species, inducing polarity in nearby atoms which stabilizes the interaction species. The interaction distance between hydrogen and TM is 1.48 Å in H/Fe@B8, 1.44 Å in H/Co@B8, 2.06 Å in H/Ni@B8, 2.09 Å in H/Cu@B8, and 1.69 Å in H/Zn@B8 complexes (see in Table 3). The short bond distance *i.e.* 1.44, 1.48 and 1.69 Å in H/Co@B8, H/Fe@B8, and H/Zn@B8 complexes confirmed the more effective hydrogen adsorption. In H/Ni@B8 and H/Cu@B8 complexes, hydrogen is adsorbed on boron instead TM having bond distance of 1.35 and 1.19 Å, respectively.

The E_{int} of hydrogen with isolated B8 is −1.82 eV. A variational trend of E_{int} is observed after H adsorption with TM@B8 (TM = Zn, Cu, Co, Ni, Fe) complexes. The E_{int} of H atom in H/Fe@B8, H/Co@B8, H/Ni@B8, H/Cu@B8, and H/Zn@B8 complexes is 0.02, −0.01, −0.04, −0.05 and −0.02 eV, respectively (see Table 3). The reasonable thermodynamic stability is seen for H/Cu–B8 complex (E_H = −0.05 eV) which is also justified from the less bond distance of 1.19 Å between H and B atoms in respective complex. The interaction energy increases with decreasing interaction distance. You *et al.* worked on Ni doped phosphide, and they observed almost similar hydrogen adsorption energy trend.[46] These results are also similar to results of transition metals adsorbed $Mg_{12}O_{12}$ complexes which were suggested as potential SACs toward HER.[45] Afterward, these complexes are also optimized with hydrogen adsorption under neutral conditions. The E_H values of H@B8 (−1.18 eV), H/Ni@B8 (−1.36 eV), H/Cu@B8 (−1.46 eV) and H/Zn@B8 (−0.05 eV) show the high thermodynamically stable of all the catalysts. Meanwhile, the E_{HOMO} of H/Fe@B8 and H/Co@B8 are 0.03 and 0.15 eV, respectively (see Table S1, ESI†).

Variations in energies of frontier molecular orbitals in TM@B8 complexes is observed after hydrogen adsorption. HOMO energy in H/Zn@B8, H/Cu@B8, H/Ni@B8, H/Co@B8 and H/Fe@B8 complexes is −8.05, −8.40, −7.96, −8.47, and

Table 3 NBO charge value on TM (Q_{TM} in $|e|$), LUMOs energy (E_{LUMO} in eV), HOMOs energy (E_{HOMO} in eV), the HOMO–LUMO gap (E_{H-L}, in eV), NBO charge value on hydrogen (Q_H in $|e|$), bond distance between hydrogen & TM (D_{H-TM} in Å) and boron & hydrogen atom (D_{B-H} in Å), adsorption energy of hydrogen in TM@B8 (E_H in eV) complexes and Gibb's free energy (ΔG_H in eV) of hydrogen adsorbed TM@B8 (TM = Zn, Cu, Co, Ni, Fe) complexes

System	Q_{TM}	E_{LUMO}	E_{HOMO}	E_{H-L}	Q_H	D_{H-TM}	D_{B-H}	D_{B-B}	E_H	ΔG_H
H@B8	—	−1.24	−7.88	6.64	0.03	—	1.52	1.38	−2.37	0.76
H/Fe@B8	−0.70	−1.21	−8.56	7.35	0.14	1.48	2.67	1.56	0.02	0.42
H/Co@B8	−1.34	−2.36	−8.47	6.11	0.40	1.44	2.66	1.56	−0.01	0.16
H/Ni@B8	−0.10	−2.54	−7.96	5.42	0.20	2.06	1.35	1.56	−0.04	−1.23
H/Cu@B8	0.31	−2.45	−8.40	5.96	0.07	2.09	1.19	1.59	−0.05	−1.13
H/Zn@B8	0.57	−3.76	−8.05	4.29	−0.32	1.69	3.35	1.56	−0.02	−0.28

−8.56 eV, respectively. The energy of LUMO in H/Zn@B8, H/Cu@B8, H/Ni@B8, H/Co@B8 and H/Fe@B8 complexes is −3.76, −2.45, −2.54, −2.36 and −1.21 eV, respectively. The E_{H-L} is increased after hydrogen adsorption in TM@B8 complexes except H/Zn@B8. The smallest E_{H-L} is observed for H/Zn@B8 (4.29 eV), followed by H/Ni@B8 (5.42 eV), H/Cu@B8 (5.96 eV) and H/Co@B8 (6.11 eV) complexes (see Table 3). The E_{H-L} of H/Fe@B8 is increased to 7.35 eV. A similar trend of change in E_{H-L} gap was observed in TM doped MoSSe complexes by Deng *et al.*[47] which justifies the validity of our results. E_{H-L} g of H/Zn@B8 complex is the lowest one (4.29 eV) as compared to H/B8 complex. The isodensity in HOMO orbitals in H adsorbed complexes is located on the bonds between the boron and the interaction sites of the boron ring with the transition metals. The isodensity in LUMO orbitals is primarily concentrated on the boron atoms of the B8 ring, with small amounts on the transition metals and hydrogen atoms in each complex (see Fig. S2†).

The NBO charge on H in H/Fe@B8, H/Co@B8, H/Ni@B8 and H/Cu@B8 complexes is 0.14, 0.40, 0.20 and 0.07$|e|$, respectively indicating the shifting of electronic density from hydrogen toward TM@B8 complexes. The highest charge transfer of 0.40$|e|$ is observed in H/Co@B8. In H/Zn@B8 complex, charge on H is −0.32$|e|$, which indicated the charge transfer toward the hydrogen atom. Specifically, 0.57, 0.31, −0.10, −1.34, and −0.70$|e|$ charges are seen on the TMs of the H/Zn@B8, H/Cu@B8, H/Ni@B8, H/Co@B8, and H/Fe@B8 complexes (see Table 3). Co metal in H/Co@B8 has the highest NBO charge of −1.34$|e|$, while Ni metal in H/Ni@B8 has the lowest charge transfer (−0.10$|e|$) in H/Ni@B8. Variation in the NBO charge reflects the interactions between H and designed TM@B8 (T = Zn, Cu, Co, Ni, Fe) complexes. The interaction distance between Co metal and hydrogen is the shortest one compared to other complexes. This represents more interaction, which is also cleared from the highest negative charge on Co (−1.34$|e|$). The hydrogen attached to the Co has the higher positive charge (0.40$|e|$) which shows the charge transfer from hydrogen to Co metal in H/Co@B8 complex.

Graphics of EDD analysis showing qualitative indication of charge transfer between TM@B8 and hydrogen are shown in Fig. 4. In H/TM@B8 complexes, purple color on TM@B8 represents the charge transfer from the TM@B8 toward H. The cyan blue color surface on the interacting side of the H which illustrates acceptance of charge by H. particularly, in Fe@B8 Co@B8, Ni@B8 and Cu@B8 complexes, purple color on hydrogen represents the charge transfer from the hydrogen toward the TM@B8. The cyan blue color surface on the interacting side of the TM@B8 which illustrates acceptance of charge by TM@B8 (Fig. S3†).

Total density of states (TDOS) spectral analysis is performed to study the energy states of occupied and unoccupied molecular orbitals. The HOMOs and LUMOs are represented on the right and left sides of each spectrum, respectively (see Fig. 6 and S4†). New energy states are generated in all TM@B8 (TM = Zn, Cu, Co, Ni, Fe) complexes due to charge transfer from TM to B8 complexes. Furthermore, TDOS spectra verified the change in E_{H-L} on the basis of the HOMOs and LUMOs energy states. Prominent variations in energy states of TDOS spectra of hydrogen-adsorbed TM@B8 complexes (H/TM@B8) are seen. Among all these complexes, the H/Zn@B8 complex exhibits a significant variation in the energy states, with the lowest energy gap (E_{H-L}) of 4.29 eV. The peak intensity in spectrum indicates the extent of electronic contribution in each complex. The highest intensity of peaks is seen in H/TM@B8 complexes, followed by TM@B8 complexes and then least in pure B8 spectrum. This analysis depicts the higher extent of electronic contribution in H/TM@B8 complexes. The average electronic contribution is seen in TM@B8 complexes in comparison to H/TM@B8 complexes. The overlapping of the peaks in each spectrum illustrates the stronger electronic interactions between these interacting species in both TM@B8 and H/TM@B8 complexes. These results are very similar to findings of Kosar *et al.* work on HER of TM doped $Si_{12}C_{12}$ complexes.[48]

The nature of interactions is elucidated from non-covalent interaction (NCI) analysis through spotting low and high electronic density regions in complexes. Three-dimensional NCI and two-dimensional reduced density gradient (RDG) graphs of H/TM@B8 complexes, are shown in Fig. 7 and ESI Fig. S5.† 3D-NCI and 2D-RDG graphs interactions are represented by colorful patches and spikes, respectively. These colorful patches and spikes indicate the presence of different types of interactions. Based on this qualitative analysis in both types of NCI and RDG graphs; blue, red and green colors indicate strong hydrogen bonding, repulsive forces, and weak van der Waals forces. In our current study, the red color patches (3D-NCI) and spikes (2D-RDG graphs) show repulsion between the boron atoms of the pure B8 nanocluster. In TM@B8 and H/TM@B8 (TM = Zn, Cu, Co, Ni, Fe) complexes, the dominant factors are the blue and red

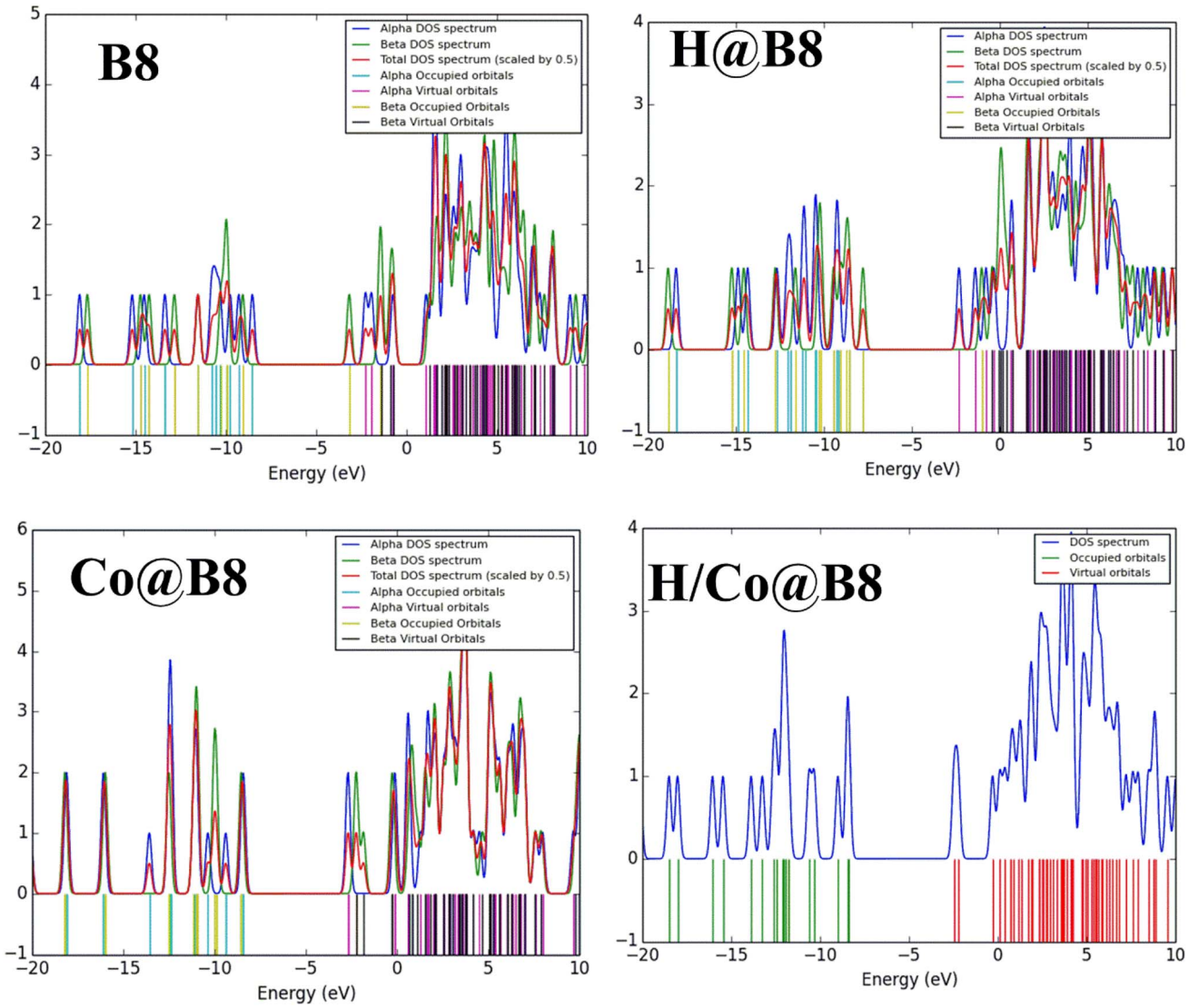

Fig. 6 Total density of states (DOS) spectra of pure B8 and H@B8, Co@B8 and H/Co@B8 complexes.

colors in 3D-NCI and 2D-RDG graphs, respectively. Red color indicates steric repulsion between the boron atoms in the B8 nanocluster in both TM@B8 and H/TM@B8 (T = Zn, Cu, Co, Ni, Fe) complexes. While blue color indicates hydrogen bonding in H/TM@B8 (TM = Zn, Cu, Co, Ni, Fe) complexes. Green reflects the presence of noncovalent interactions in H/TM@B8 (TM = Zn, Cu, Co, Ni, Fe) complexes.

For quantitative analysis 2D-RDG graphs are used, the Laplacian of density ($\nabla^2\rho$) is used to differentiate among various types of bonding. For covalent contacts, negative contributions predominate, resulting in a negative Laplacian value. For weaker noncovalent interactions, positive contribution is dominant in the interatomic region of the Laplacian. The negative sign of λ_2 is a key indicator of interactions; thus, the sign of λ_2 can distinguish between bonded interactions ($\lambda_2 < 0$) and non-bonded interactions ($\lambda_2 > 0$). The λ_2 and the density are important parameters to distinguish various kinds of non-covalent interactions. Negative values between −0.020 to −0.035, shown in blue on the left side of the RDG graph, indicate strong hydrogen bonding. Positive values above 0.010, shown in red, indicate repulsive forces. The sign(λ_2)ρ values in the range of −0.01 to −0.01, shown in green, indicate weak van der Waals forces in H/TM@B8 complexes. Both blue and red colors are seen in both 3D-NCI figures and 2D-RDG graphs illustrate strong hydrogen bonding and repulsion forces. The green spikes are only seen in the 2D-RDG graphs and represent weak van der Waals interactions in all H/TM@B8 (TM = Zn, Cu, Co, Ni, Fe) complexes. As we moved towards the 3D-RDG graphs of H/TM@B8 complexes, the more prominent blue, green and red spikes are observed indicating the stronger hydrogen bonding, repulsive and van der Waals interactions within each complex after hydrogen adsorption. These results are similar to Kosar *et al.* work on HER on TM doped $Si_{12}C_{12}$ complexes.[48]

3.4 Catalytic activity of TM@B8 complexes toward HER

For an ideal HER catalytic activity, the ΔG_H value should be closer to zero. The catalytic activity as single-atom catalysts

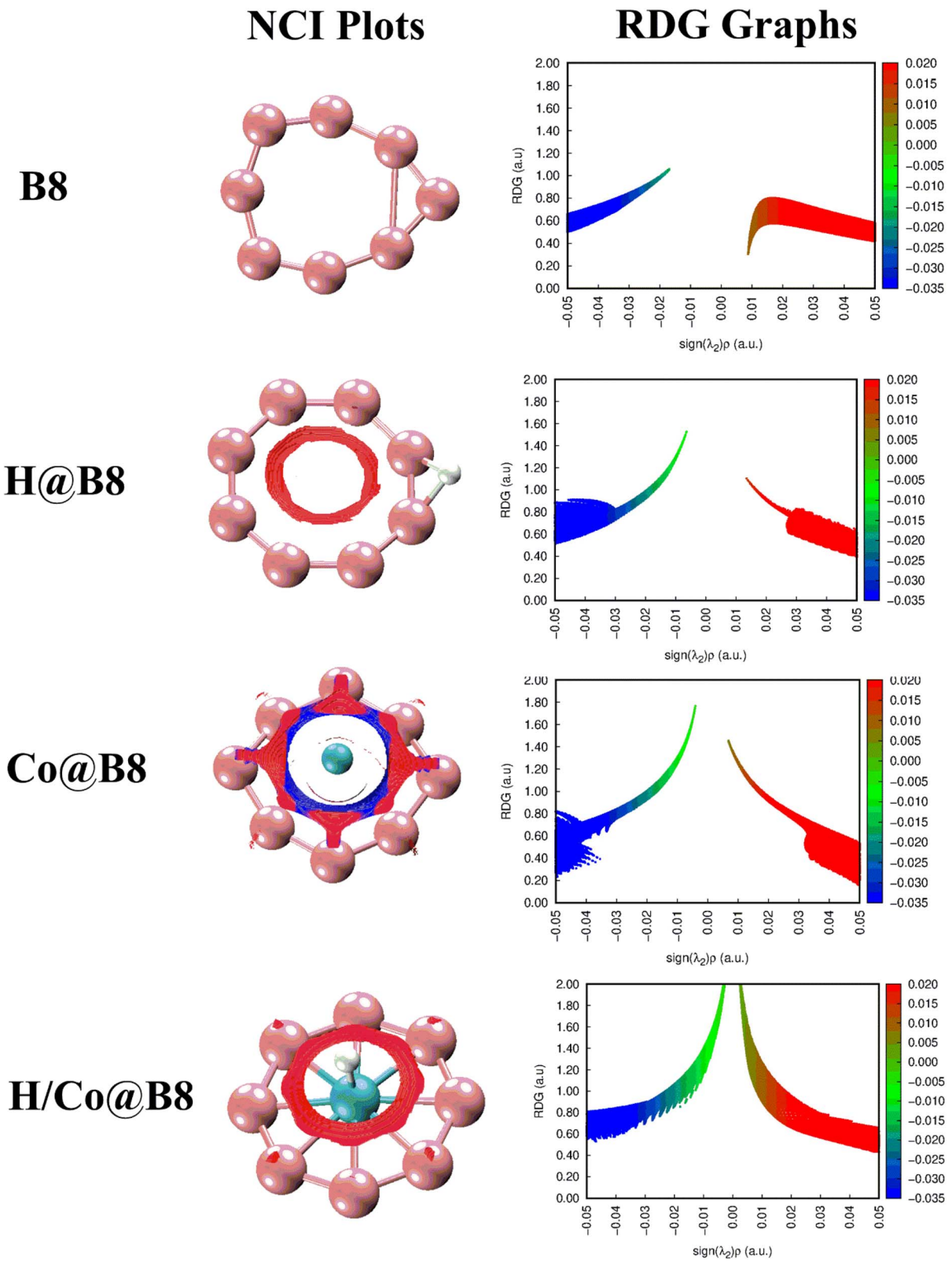

Fig. 7 3D-RDG graph (right side) and 2D-NCI plots (left side) and of pure B8, H@B8, Co@B8 and H/Co@B8.

(SACs) is evaluated by calculating the change in Gibbs free energy during HER. Doping of transition metals on the B8 nanocluster is supposed to enhance the catalytic efficiency of B8 toward hydrogen evolution reaction. The graphical comparison of change in Gibbs free energy of all designed catalysts is shown in Fig. 8. ΔG_H values near zero indicate excellent performance

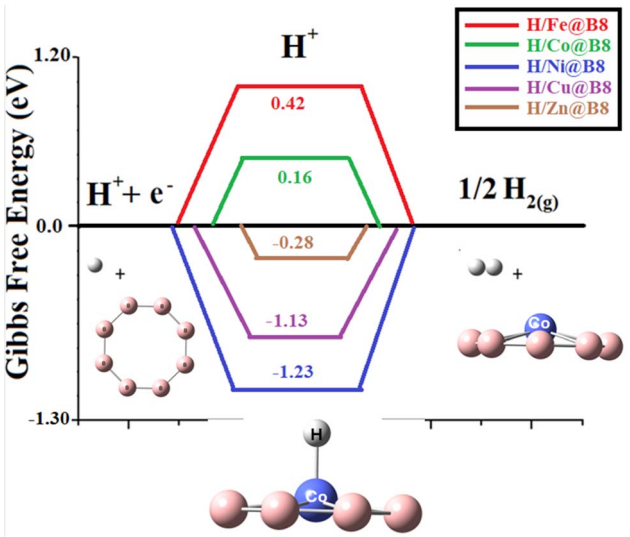

Fig. 8 Comparative graph of modelled HER catalysts (TM@B8, TM = Zn, Cu, Co, Ni, Fe) with calculated Gibb's free energies.

for HER activity. Table 3 lists the ΔG_H values for HER: −0.28, −1.13, −1.23, 0.16, and 0.42 eV for H/Zn@B8, H/Cu@B8, H/Ni@B8, H/Co@B8, H/Fe@B8 complexes, respectively. Overall, Co@B8 exhibits excellent HER activity with a ΔG_H value of 0.16 eV, which is near zero. Ni@B8, with a ΔG_H value of −1.23 eV, shows the lowest HER activity among the designed TM@B8 complexes.

One of the factors that affects the change in Gibbs free energy is the interaction energy of hydrogen. The effective catalyst must have an optimal balance of hydrogen adsorption and desorption (E_{int} not so much high and not so low). Similarly, ΔG_H value should also be optimal near to zero according to Tafel step. This is obeyed by Co@B8 having E_{int} of 0.01 eV and ΔG_{H*} value of 0.16 eV. The Fe@B8 exhibits weak hydrogen adsorption and has E_{int} of 0.02 eV. Due to this reason its ΔG_H is 0.42 eV which makes the adsorption process energetically unfavorable. Remaining complexes including Ni@B8, Cu@B8 and Zn@B8 show strong hydrogen adsorption as depicted from their E_{int} values of −0.04, −0.05 and −0.02. Their (Ni@B8, Cu@B8 and Zn@B8) ΔG_H are also high and ranges from −0.28 to −1.23 which causes impeding desorption.[49] Among all complexes, Co@B8 acts as an effective catalyst for the next generation HER process.[50–52] This Gibb's free energy value is comparable to the reported values of various complexes in literature. A detailed comparison of this work is given with the literature in Table 4.

HER catalytic activity of TM@B8 complexes is also investigated under neutral condition which reported as the best approach both experimentally and theoretically.[53] The ΔG_H values of HER under neutral conditions are −1.43, 0.82, 0.33, −1.09, −1.16, and 0.76 eV for H@B8, H/Fe@B8, H/Co@B8, H/Ni@B8, H/Cu@B8, H/Zn@B8 (see Table S1, ESI†). Overall, Co@B8 exhibits excellent HER activity with a ΔG_H value of 0.33 eV in water as solvent. Cu@B8, with a ΔG_H value of −1.16 eV, shows the lowest hydrogen adsorption among the designed TM@B8 catalysts.

Table 4 Comparative analysis of our best designed single atom catalysts with reported SACs for HER activity

Complexes	ΔG_H (eV)	References
Fe@GDY	0.22	54
Fe@MO_2CO_2, Fe@Cr_2CO_2	0.16, −0.12	55
Fe@SnO	−0.44	56
1T-MoS_2	0.07	57
Co@graphene	0.13	58
Re@MoS_2	−0.43	59
Nb@MoS_2	0.06	60
GeP_3	0.02	61
NiPd–gCN	−0.15	62
$MoSi_2N_4$/MoSX (X = S, Se)	∼0	63
Ti@MoS2	−0.63	64
Pt@GDY, Ni@GDY	0.01, 0.46	65
NiCoP on Co, P sites	0.08, 0.12	66
Co@B8	0.16	Current work

3.5 Catalytic activity of TM@B8 toward oxygen evolution reaction (OER)

Oxygen evolution reaction (OER) potential of designed complexes is also investigated. OER is an essential process during the electrocatalysis of water splitting. Generally, OER proceeds through four steps proton coupled electron transfer (PCET) process. In PCET, three intermediates play a pivotal role including OH*, O* and OOH* with substrate. All the newly designed intermediates (OH*, O* and OOH* with B8) in this study are optimized at same ωB97XD with 6-31+G(d,p) using three lower spin states starting with default spin state. The most stable spin state of intermediate for each step is given in Table 5, and pictorial representation is given in Fig. 9. The rest of the results are given in Table S2 and Fig. S6 (ESI†). The change in Gibb's free energies of each PCET step (ΔG_I − ΔG_{IV}) is calculated to know about the kinetics of the OER. The change in Gibb's free energies is divided into equal values in four PCET steps for OER of an ideal catalyst. The total ΔG of PCET is 4.92 eV where the ΔG of each step is 1.23 eV. The variation in the thermodynamic stabilities between the intermediates of SACs causes variation in the Gibb's free energies and over potential of each PCET steps.[67,68] In our current study, total ΔG is 4.42 eV and ΔG ((I)–(IV)) of each step is 1.10 eV. These computational values are in close agreement with experimental values which

Table 5 The most stable spin states for the intermediates of OER, potential determining steps (PDS) along with respective Gibb's free energy change (ΔG_{max} in eV) and overpotential (η_{OER} in V)

	Intermediates with stable spin states					
Catalysts	* + OH*	* + O	* + OOH	PDS	ΔG_{max}	η_{OER}
Fe@B8	Doublet	Triplet	Doublet	(III)	2.24	1.14
Co@B8	Triplet	Sextet	Triplet	(III)	2.71	1.60
Ni@B8	Quartet	Quintet	Quartet	(I)	1.69	0.59
Cu@B8	Singlet	Sextet	Triplet	(II)	5.91	4.80
Zn@B8	Doublet	Quintet	Doublet	(III)	3.30	2.20

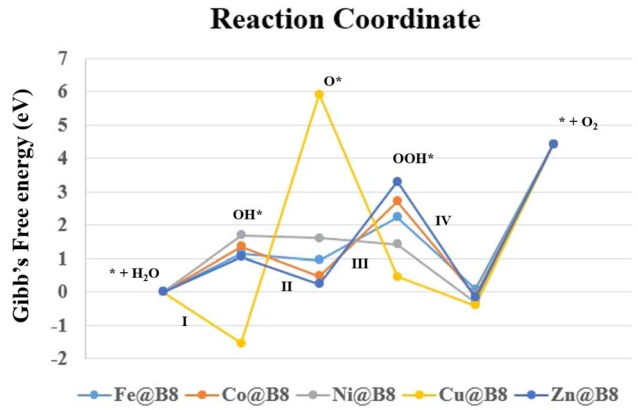

Fig. 9 Comparative graphs of Modelled OER catalytic activity of (TM@B8, TM = Zn, Cu, Co, Ni, Fe) with calculated Gibb's free energies.

are accepted in literature.[69,70] The change in Gibb's free energies of the total OER is the summation of the four important steps which differ from each other based on thermodynamic stability of the intermediates. Some steps are endergonic in nature and others are exergonic in nature. Although it is desirable to have a reaction with endergonic behavior. Gibb's free energies values are used to calculate the overpotential values (see in Table 5). The higher Gibb's free energies cause increase in overpotential which is the main cause of high potential in OER.[65,71] Table 5 illustrates that the desirable potential determination step (PDS) of Fe@B8, Co@B8, and Zn@B8 is step (III). PDS of Ni@B8 and Cu@B8 are (I) and (II), respectively. The best catalytic potential is observed for Fe@B8 with ΔG_{PDS} and η_{OER} values of 2.24 eV and 1.14 V, respectively. Because the 1.14 eV of Fe@B8 is seen close to the 1.10 eV per step value. The same kind of results are seen in previously published literature.[72]

Conclusively, Fe@B8 show best performance for OER with ΔG_{PDS} and η_{OER} values of 2.24 eV and 1.14 V, respectively which is close to the 1.10 eV per step value of PCET. The Co@B8 exhibits excellent HER activity with a ΔG_H value of 0.16 eV, which is near zero.

4 Conclusion

Late first row transition metal-adsorbed B8 complexes are investigated as single-atom catalysts (SACs) toward HER application. Various properties including interaction energy (E_{int}), energies of frontier molecular orbitals (FMOs), natural bonding orbital (NBO) charges, TDOS spectral analysis, and non-covalent interaction (NCI) of considered complexes are explored. These properties helped in describing the thermodynamic stability, electronic reactivity and types of bonding in TM@B8 complexes. The doping of TM with B8 nanocluster and further the H adsorption significantly improved stability of complexes. The $E_{int.}$ of all H/TM@B8 (T = Zn, Cu, Co, Ni, Fe) complexes are observed in the range of 0.02 to −0.05 eV, indicating thermodynamic feasibility upon complexation. NBO calculations revealed charge transfer from the adsorbed transition metals to the B8 nanocluster. After hydrogen adsorption, NBO charges transfer to hydrogen and *vice versa*, highlighting the adsorption properties of hydrogen. The HOMO–LUMO energy gap for transition metal-adsorbed complexes ranges from 5.07–7.32 eV, but this gap reduces up to 4.29 eV, after hydrogen adsorption, confirming the improved conductivity of the TM@B8 complex. DOS spectra illustrated the energy states of the molecular orbitals and the extent of electronic contribution in these complexes. NCI plots further explained the existence of hydrogen bonding, noncovalent interactions, and steric repulsion in H/TM@B8 complexes. Gibbs free energy and entropy calculation are instrumental in explaining HER activity. Conclusively, The Co@B8 exhibits excellent HER activity with a ΔG_H value of 0.16 eV, which is near zero in gas phase. Fe@B8 show the best performance for OER with ΔG_{PDS} and η_{OER} values of 2.24 eV and 1.14 V, respectively which is close to the 1.10 eV per step value of PCET. These outcomes show the promising potential of TM@B8 catalysts for both HER and OER process.

Data availability

The data that support the findings of this study are available from the corresponding author, [mahmood@cuiatd.edu.pk (T. M.)], upon reasonable request.

Author contributions

Naveen Kosar: simulation, logical methodology, data analysis, writing the original manuscript. Tariq Mahmood: supervision, software, editing, review and finalizing the manuscript. Muhammad Arshad: data analysis, validation. Muhammad Imran: conceptualization, funding acquisition, project administration. Utkirjon Holikulov: resources, project administration, validation.

Conflicts of interest

The authors declare no competing and conflict of interests.

Acknowledgements

The authors acknowledge the Higher Education Commission (NRPU project; 20-16279/NRPU/HEC/2021-2020) of Pakistan. M. I. express appreciation to the Deanship of Scientific Research at King Khalid University Saudi Arabia through the research groups program under grant number R. G. P. 2/608/45. The experiments presented in this paper were carried out using the facilities of the Benefit Advanced AI and Computing Lab at the University of Bahrain {see **https://ailab.uob.edu.bh**} with support from Benefit Bahrain Company {see **https://benefit.bh**}.

References

1 V. D. Yumatov, E. A. Il'inchik and V. V. Volkov, *Russ. Chem. Rev.*, 2003, **72**, 1011–1034.
2 R. N. Grimes, *J. Chem. Educ.*, 2004, **81**, 657.
3 M. Atiş, C. Özdoğan and Z. B. Güvenç, *Int. J. Quantum Chem.*, 2007, **107**, 729–744.

4 J. Plesek, *Chem. Rev.*, 1992, **92**, 269–278.
5 O. Mishima, J. Tanaka, S. Yamaoka and O. Fukunaga, *Science*, 1987, **238**, 181–183.
6 I. A. Howard and A. K. Ray, *Z. Phys. D:At., Mol. Clusters*, 1997, **42**, 299–301.
7 M. Atis, C. Ozdosan and Z. B. Guvenc, *Chin. J. Chem. Phys.*, 2009, **22**, 380–388.
8 Z. Cui, C. Chen, Q. Wang, L. Zhao, M. Wang and Y. Ding, *New J. Chem.*, 2020, **44**, 17705–17713.
9 W.-L. Li, X. Chen, T. Jian, T.-T. Chen, J. Li and L.-S. Wang, *Nat. Rev. Chem*, 2017, **1**, 0071.
10 W.-J. Chen, M. Kulichenko, H. W. Choi, J. Cavanagh, D.-F. Yuan, A. I. Boldyrev and L.-S. Wang, *J. Phys. Chem. A*, 2021, **125**, 6751–6760.
11 Y. Luo, F. Chen, H. Zhang, J. Liu and N. Liu, *J. Org. Chem.*, 2023, **88**, 15717–15725.
12 X.-F. Yang, A. Wang, B. Qiao, J. Li, J. Liu and T. Zhang, *Acc. Chem. Res.*, 2013, **46**, 1740–1748.
13 Z. Chen, J. Liu and K. P. Loh, *Acc. Mater. Res.*, 2023, **4**, 27–41.
14 S. Wang, H. Gao, L. Li, K. S. Hui, D. A. Dinh, S. Wu, S. Kumar, F. Chen, Z. Shao and K. N. Hui, *Nano Energy*, 2022, **100**, 107517.
15 S. Sun, G. Zhang, N. Gauquelin, N. Chen, J. Zhou, S. Yang, W. Chen, X. Meng, D. Geng, M. N. Banis, R. Li, S. Ye, S. Knights, G. A. Botton, T.-K. Sham and X. Sun, *Sci. Rep.*, 2013, **3**, 1775.
16 J. Liu, X. Kong, L. Zheng, X. Guo, X. Liu and J. Shui, *ACS Nano*, 2020, **14**, 1093–1101.
17 L. Jin, C. Liu, D. Wang, M. Liu, T. G. Lee, S. G. Peera and X. Qi, *Appl. Surf. Sci.*, 2023, **610**, 155580.
18 A. Yu, N. Joshi, W. Zhang and Y. Yang, *Advanced Sensor and Energy Materials*, 2023, **2**, 100061.
19 S. Griffiths, B. K. Sovacool, J. Kim, M. Bazilian and J. M. Uratani, *Energy Res. Soc. Sci.*, 2021, **80**, 102208.
20 N. S. Lewis and D. G. Nocera, *Proc. Natl. Acad. Sci. U. S. A.*, 2006, **103**, 15729–15735.
21 N. Armaroli and V. Balzani, *Angew. Chem., Int. Ed.*, 2007, **46**, 52–66.
22 A. V. Abad and P. E. Dodds, *Energy Policy*, 2020, **138**, 111300.
23 F. Zaccaria, G. M. Rodriguez, L. Rocchigiani and A. Macchioni, *Front. Catal.*, 2022, **2**, 892183.
24 F. Abdelghafar, X. Xu, S. P. Jiang and Z. Shao, *Mater. Rep.: Energy*, 2022, **2**, 100144.
25 H. Meng, W. Zhang, Z. Ma, F. Zhang, B. Tang, J. Li and X. Wang, *ACS Appl. Mater. Interfaces*, 2018, **10**, 2430–2441.
26 A. K. Nayak, M. Verma, Y. Sohn, P. A. Deshpande and D. Pradhan, *ACS Omega*, 2017, **2**, 7039–7047.
27 R. N. Dürr, E. Stéphan, J. Leroy, F. Oswald, B. Verhaeghe and B. Jousselme, *ChemElectroChem*, 2023, **10**, e202300205.
28 N. Mahmood, Y. Yao, J. Zhang, L. Pan, X. Zhang and J. Zou, *Adv. Sci.*, 2018, **5**, 1700464.
29 J. Kim, H. Kim, W.-J. Lee, B. Ruqia, H. Baik, H.-S. Oh, S.-M. Paek, H.-K. Lim, C. H. Choi and S.-I. Choi, *J. Am. Chem. Soc.*, 2019, **141**, 18256–18263.
30 Y. Zheng, Y. Jiao, M. Jaroniec and S. Z. Qiao, *Angew. Chem., Int. Ed.*, 2015, **54**, 52–65.
31 B. E. Conway and B. V. Tilak, *Electrochim. Acta*, 2002, **47**, 3571–3594.
32 J. K. Nørskov, T. Bligaard, A. Logadottir, J. R. Kitchin, J. G. Chen, S. Pandelov and U. Stimming, *J. Electrochem. Soc.*, 2005, **152**, J23.
33 M. Gennero de Chialvo and A. Chialvo, *Electrochim. Acta*, 1998, **44**, 841–851.
34 M. Zhang, K. Zhang, X. Ai, X. Liang, Q. Zhang, H. Chen and X. Zou, *Chin. J. Catal.*, 2022, **43**, 2987–3018.
35 B. Hinnemann, P. G. Moses, J. Bonde, K. P. Jørgensen, J. H. Nielsen, S. Horch, I. Chorkendorff and J. K. Nørskov, *J. Am. Chem. Soc.*, 2005, **127**, 5308–5309.
36 T. F. Jaramillo, K. P. Jørgensen, J. Bonde, J. H. Nielsen, S. Horch and I. Chorkendorff, *Science*, 2007, **317**, 100–102.
37 Y. Zheng, Y. Jiao, Y. Zhu, L. H. Li, Y. Han, Y. Chen, A. Du, M. Jaroniec and S. Z. Qiao, *Nat. Commun.*, 2014, **5**, 3783.
38 Y. Zheng, Y. Jiao, Y. Zhu, Q. Cai, A. Vasileff, L. H. Li, Y. Han, Y. Chen and S.-Z. Qiao, *J. Am. Chem. Soc.*, 2017, **139**, 3336–3339.
39 M. Guo, M. Ji and W. Cui, *Appl. Surf. Sci.*, 2022, **592**, 153237.
40 X. Zhang, Z. Yang, Z. Lu and W. Wang, *Carbon*, 2018, **130**, 112–119.
41 R. Dennington, T. Keith and J. Millam, *GaussView 5.0*, Semichem Inc., Shawnee Mission KS, 2009.
42 M. J. Frisch, G. W. Trucks, H. B. Schlegel, G. E. Scuseria, M. A. Robb, J. R. Cheeseman, G. Scalmani, V. Barone, B. Mennucci, G. A. Petersson, H. Nakatsuji, M. Caricato, X. Li, H. P. Hratchian, A. F. Izmaylov, J. Bloino, G. Zheng, J. L. Sonnenberg, M. Hada, M. Ehara, K. Toyota, R. Fukuda, J. Hasegawa, M. Ishida, T. Nakajima, Y. Honda, O. Kitao, H. Nakai, T. Vreven, J. A. Montgomery Jr, J. E. Peralta, F. Ogliaro, M. Bearpark, J. J. Heyd Brothers, E. K. N. Kudin, V. N. Staroverov, R. K. J. Normand, K. Raghavachari, A. Rendell, J. C. Burant, S. S. Iyengar, J. Tomasi, M. C. N. Rega, J. M. Millam, M. Klene, J. E. Knox, J. B. Cross, V. Bakken, C. Adamo, J. J. R. Gomperts, R. E. Stratmann, O. Yazyev, A. J. Austin, R. Cammi, C. Pomelli, J. W. Ochterski, R. L. Martin, K. Morokuma, V. G. Zakrzewski, G. A. Voth, P. Salvador, J. J. Dannenberg, S. Dapprich, A. D. Daniels, Ö. Farkas, J. B. Foresman, J. V. Ortiz and J. D. J. F. Cioslowski, *Gaussian 09, Revision D.01*, Gaussian, Inc., Wallingford CT, 2009.
43 P. Aggarwal, D. Sarkar, K. Awasthi and P. W. Menezes, *Coord. Chem. Rev.*, 2022, **452**, 214289.
44 Y. Yang, J. Liu, F. Liu, Z. Wang and D. Wu, *J. Mater. Chem. A*, 2021, **9**, 2438–2447.
45 M. R. S. A. Janjua, *J. Phys. Chem. Solids*, 2022, **167**, 110789.
46 B. You, Y. Zhang, Y. Jiao, K. Davey and S. Z. Qiao, *Angew. Chem.*, 2019, **131**, 11922–11926.
47 C. Xiao, R. Sa, Z. Ma, Z. Cui, W. Du, X. Sun, Q. Li and H. Deng, *Int. J. Hydrogen Energy*, 2021, **46**, 10337–10345.
48 N. Kosar, S. Rafiq, K. Ayub, M. Imran and T. Mahmood, *Int. J. Hydrogen Energy*, 2024, **68**, 1219–1228.
49 M. Ren, X. Guo and S. Huang, *Appl. Surf. Sci.*, 2021, **556**, 149801.

50 Y. Cheng, X. Fan, F. Liao, S. Lu, Y. Li, L. Liu, Y. Li, H. Lin, M. Shao and S.-T. Lee, *Nano Energy*, 2017, **39**, 284–290.
51 D. Chodvadiya, P. K. Jha and B. Chakraborty, *Int. J. Hydrogen Energy*, 2022, **47**, 41733–41747.
52 D. Chodvadiya, B. Chakraborty and P. K. Jha, *Int. J. Hydrogen Energy*, 2023, **48**, 18326–18337.
53 Z. Zhou, Z. Pei, L. Wei, S. Zhao, X. Jian and Y. Chen, *Energy Environ. Sci.*, 2020, **13**, 3185–3206.
54 W. Zhou, Z. Jiang, M. Chen, Z. Li, X. Luo, M. Guo, Y. Yang, T. Yu, C. Yuan and S. Wang, *Chem. Eng. J.*, 2022, **428**, 131210.
55 L. Sun, B. Wang and Y. Wang, *ACS Appl. Mater. Interfaces*, 2020, **12**, 21808–21817.
56 X. Li, P. Cui, W. Zhong, J. Li, X. Wang, Z. Wang and J. Jiang, *Chem. Commun.*, 2016, **52**, 13233–13236.
57 K. Zhang, B. Jin, Y. Gao, S. Zhang, H. Shin, H. Zeng and J. H. Park, *Small*, 2019, **15**, 1804903.
58 M. D. Hossain, Z. Liu, M. Zhuang, X. Yan, G. Xu, C. A. Gadre, A. Tyagi, I. H. Abidi, C. Sun, H. Wong, A. Guda, Y. Hao, X. Pan, K. Amine and Z. Luo, *Adv. Energy Mater.*, 2019, **9**, 1803689.
59 X. Zhai, L. Li, X. Liu, Y. Li, J. Yang, D. Yang, J. Zhang, H. Yan and G. Ge, *Nanoscale*, 2020, **12**, 10035–10043.
60 K. S. Joseph and S. Dabhi, *Electrochim. Acta*, 2024, **505**, 144968.
61 H.-H. Wu, H. Huang, J. Zhong, S. Yu, Q. Zhang and X. C. Zeng, *Nanoscale*, 2019, **11**, 12210–12219.
62 X. Liu, D. K. Hoang, Q. A. T. Nguyen, D. Dinh Phuc, S.-G. Kim, P. C. Nam, A. Kumar, F. Zhang, C. Zhi and V. Q. Bui, *Nanoscale*, 2024, **16**, 13148–13160.
63 A. Jalil, T. Zhao, A. Kanwal and I. Ahmed, *Chem. Eng. J.*, 2023, **470**, 144239.
64 H. Guo, L. Li, X. Wang, G. Yao, H. Yu, Z. Tian, B. Li and L. Chen, *ACS Appl. Mater. Interfaces*, 2019, **11**, 36506–36514.
65 T. He, S. K. Matta, G. Will and A. Du, *Small Methods*, 2019, **3**, 1800419.
66 C. Liu, G. Zhang, L. Yu, J. Qu and H. Liu, *Small*, 2018, **14**, 1800421.
67 E. Sargeant, F. Illas, P. Rodríguez and F. Calle-Vallejo, *J. Electroanal. Chem.*, 2021, **896**, 115178.
68 S. Tosoni, G. Di Liberto, I. Matanovic and G. Pacchioni, *J. Power Sources*, 2023, **556**, 232492.
69 A. Allangawi, T. Mahmood, K. Ayub and M. A. Gilani, *Mater. Sci. Semicond. Process.*, 2023, **153**, 107164.
70 S. Lu, H. L. Huynh, F. Lou, K. Guo and Z. Yu, *Nanoscale*, 2021, **13**, 12885–12895.
71 J. K. Nørskov, J. Rossmeisl, A. Logadottir, L. Lindqvist, J. R. Kitchin, T. Bligaard and H. Jónsson, *J. Phys. Chem. B*, 2004, **108**, 17886–17892.
72 S. H. Talib, Z. Lu, X. Yu, K. Ahmad, B. Bashir, Z. Yang and J. Li, *ACS Catal.*, 2021, **11**, 8929–8941.